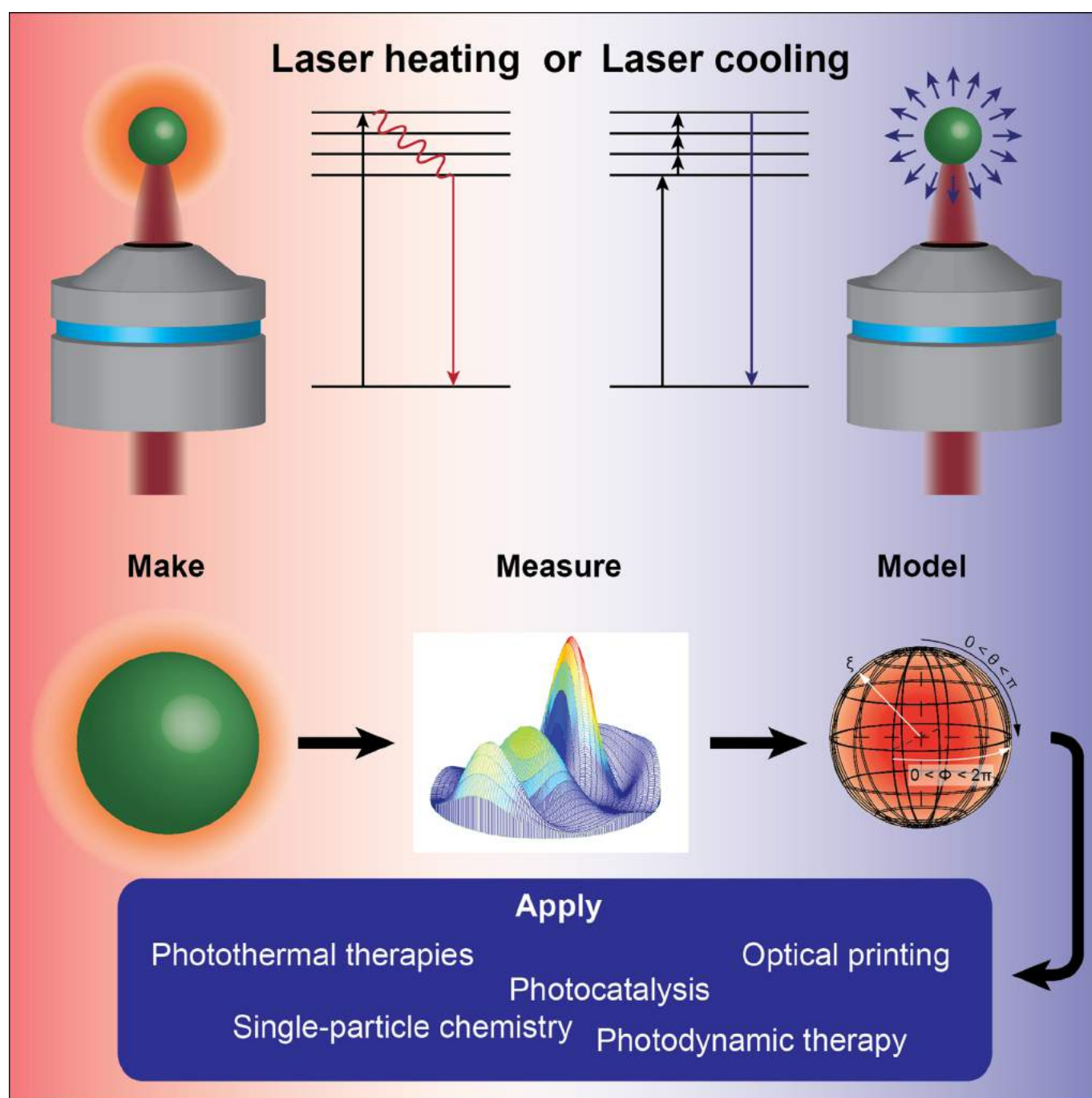


## Heat Transfer

# Photothermal Heating and Cooling of Nanostructures

Matthew J. Crane,<sup>[a]</sup> Xuezhe Zhou,<sup>[b]</sup> E. James Davis,<sup>[a]</sup> and Peter J. Pauzauskie<sup>\*,[b, c]</sup>



**Abstract:** A vast range of insulating, semiconducting, and metallic nanomaterials have been studied over the past several decades with the aim of understanding how continuous-wave or pulsed laser radiation can influence their chemical functionality and local environment. Many fascinating observations have been made during laser irradiation including, but not limited to, the superheating of solvents, mass-transport-mediated morphology evolution, photodynamic therapy, morphology dependent resonances, and a range of phase transformations. In addition to laser heating, recent experiments have demonstrated the laser cooling of nano-

scale materials through the emission of upconverted, anti-Stokes photons by trivalent rare-earth ions. This Focus Review outlines the analytical modeling of photothermal heat transport with an emphasis on the experimental validation of anti-Stokes laser cooling. This general methodology can be applied to a wide range of photothermal applications, including nanomedicine, photocatalysis, and the synthesis of new materials. The review concludes with an overview of recent advances and future directions for anti-Stokes cooling.

## 1. Introduction

The photothermal excitation of inorganic nanostructures has attracted a significant amount of interest in recent years due to applications in the optical ablation of solid tumors,<sup>[1–3]</sup> the theory of hot Brownian motion,<sup>[4]</sup> the modification of metal nanostructures,<sup>[5,6]</sup> the production of contrast agents,<sup>[7]</sup> the optical printing of materials,<sup>[8,9]</sup> the growth of semiconductor nanowires,<sup>[10–14]</sup> nanoscale photophoretic propulsion,<sup>[15,16]</sup> the thermal actuation of myosin V motor proteins,<sup>[17]</sup> and, recently, the laser cooling of nanomaterials.<sup>[18,19]</sup> Electromagnetic theory and analytical heat transport solutions exist or are under development to describe many of these applications. Despite this, many publications lack analyses of heat transport, which offer a convenient method to quantify results and test hypotheses and observations.

This Focus Review begins with an overview of recent progress in modeling the generation and diffusion of heat within nanoscale materials during laser irradiation. First, photothermal heating theory is discussed in the context of the partial differential energy equation which is solved analytically using a series solution based on a classical product of eigenfunctions. Second, we present guidelines to apply this theory for laser cooling. Heat generation within nanostructures is modeled by relating the incident, external electromagnetic field of the exciting laser to the resulting internal electromagnetic field within the particle. The generation of heat is based on the

Joule heating of conduction electrons that are driven by the oscillating internal field.<sup>[20,21]</sup> Care is taken to describe how boundary conditions,<sup>[22–24]</sup> size-dependent nanoscale thermal conductivity parameters,<sup>[25–27]</sup> interfacial heat-transfer coefficients,<sup>[28–32]</sup> and morphology-dependent cavity (Mie) resonances or localized surface plasmon resonances,<sup>[33–39]</sup> impact the diffusion of heat within and from inorganic nanostructures. The methods presented here are general and will be of use for understanding heat transfer in a range of nanoscale materials, including the characteristic experimental time scales required to reach thermal steady state conditions,<sup>[40]</sup> and the aforementioned applications. In addition to laser-heating, the review includes an overview of an emerging direction of solid-state laser-refrigeration of inorganic nanomaterials based on the up-conversion emission of rare-earth ions.<sup>[41,42]</sup> More recently solid-state laser-refrigeration has led to the first experimental demonstrations of cold Brownian motion,<sup>[18,19]</sup> since Einstein's seminal work describing Brownian motion at thermal equilibrium.<sup>[43,44]</sup>

## 2. Photothermal Heating Theory

### 2.1. The Energy Equation

The energy equation governing the temperature distribution in a nanomaterial with constant thermal properties is given by [Eq. (1)]

$$\rho C \frac{\partial T}{\partial t} = \kappa \nabla^2 T + \dot{Q} \quad (1)$$


in which  $\rho$  is the density,  $C$  is the specific heat per unit mass,  $\kappa$  is the thermal conductivity,  $T$  is the temperature,  $t$  is time, and  $\dot{Q}$  is the rate of heat generation (or depletion) per unit volume. The Laplacian,  $\nabla^2$ , should be written in terms of the appropriate coordinate system such as presented by Bird et al.<sup>[45]</sup> for Cartesian, cylindrical, and spherical coordinates.

Although the thermal properties are temperature dependent,<sup>[46]</sup> it is convenient to evaluate them at the mean temperature of the material to develop useful analytical solutions of the governing equation. Numerical solutions are needed to ac-

[a] Dr. M. J. Crane, Prof. E. J. Davis  
Department of Chemical Engineering  
University of Washington  
Seattle, WA (USA)

[b] Dr. X. Zhou, Prof. P. J. Pauzauskie  
Department of Materials Science & Engineering  
University of Washington  
Seattle, WA (USA)

[c] Prof. P. J. Pauzauskie  
Physical and Computational Sciences Directorate  
Pacific Northwest National Laboratory  
Richland, WA (USA)  
E-mail: peterpz@uw.edu

 The ORCID identification number(s) for the author(s) of this article can be found under:  
<https://doi.org/10.1002/asia.201800251>.

count for large changes in the thermal properties with temperature.

During laser heating of the nanomaterial, the heat source depends on the laser irradiance, its polarization, and the optical properties of the material. It is given by<sup>[47]</sup> [Eq. (2)]

$$\dot{Q} = \frac{4\pi n_{re} n_{im}}{\lambda_0 Z_0} (E \cdot E^*) = \frac{2n_{re} k_{im}}{Z_0} (E \cdot E^*), \quad (2)$$

in which  $E$  is the electric vector,  $E^*$  is its complex conjugate,  $Z_0$  is the vacuum impedance (376.73 ohms), and  $\lambda_0$  is the wavelength of the laser light in vacuo. The heat source,  $\dot{Q}$ , also referred to as the source function, represents the volumetric power absorbed within a material from a light source. The complex refractive index,  $n$ , and the complex wave number,  $k$ , are defined by [Eq. (3)]

$$k = k_{re} - ik_{im} = \frac{2\pi}{\lambda_0} n = \frac{2\pi}{\lambda_0} (n_{re} - in_{im}). \quad (3)$$

We note that  $k_{im}$  and  $n_{im}$  are related to the absorption coefficient by  $\alpha = 2k_{im} = 4\pi n_{im}/\lambda_0$ . With electromagnetic heating of spheres and of long circular cylinders the source function can be determined by application of Mie theory.<sup>[47,35]</sup> Bohren and Huffman<sup>[35]</sup> have provided codes for calculating light scattering and absorption for spheres, coated spheres and normally illuminated infinite cylinders. Numerical methods are available for light scattering characteristics of particles with arbitrary shapes. These include the discrete-dipole approximation<sup>[37,39,49,50]</sup> and finite-difference time-domain simulations recently implemented in an open-source software package (MEEP<sup>[51]</sup>).

The source function for spheres and cylinders that are not small compared with the wavelength of the incident irradiation have a rich structure that is strongly dependent on the size and optical properties of the nanomaterial. Figure 1 shows the electric field distribution computed by Roder et al.<sup>[52]</sup> using the solution presented by Bohren and Huffman and MEEP.

For laser cooling applications, the volumetric source term, will be negative. In addition, it must incorporate the laser cooling mechanism and efficiency as  $\dot{Q}_{cooling} = -\dot{Q}\eta$ , where  $\eta$  is the overall cooling efficiency as defined in section 3.1. We note

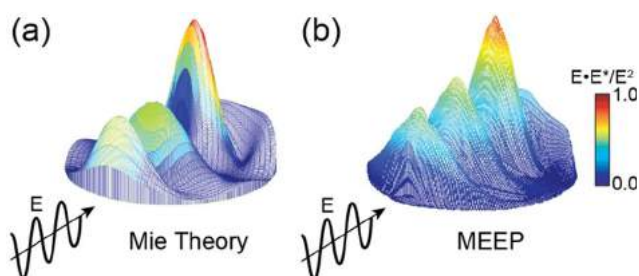


**Figure 1.** The normalized electric field distribution,  $(E \cdot E^*)/E_0^2$ , for an infinitely long 500 nm diameter silicon cylinder in water irradiated with  $\lambda_0 = 980$  nm (a) using the analytical results of Bohren and Huffman and (b) using MEEP. Figure reproduced with permission from reference [33] copyright the American Chemical Society.

that  $\eta$  includes the effects of both laser cooling and heating terms. It is important to note that for laser cooling mechanisms which involve long excited state lifetimes that compete with diffusion, for example,  $\text{Yb}^{3+}$ - $\text{Yb}^{3+}$  transfer,<sup>[18]</sup> the laser cooling source must incorporate this diffusion. This will result in a “spreading” of the source term. In materials with position-dependent doping, the effects of diffusion could be engineered

Matthew Crane received his B.S. *summa cum laude* from the Georgia Institute of Technology and recently obtained his M.S. and Ph.D. from the University of Washington in Chemical Engineering as a NDSEG fellow. He is currently a Washington Research Foundation Postdoctoral Fellow interested in ultrafast spectroscopy, photocatalysis, and defects for quantum sensing and hyperpolarization.



Xuezhe Zhou received his B.S. in Materials Science and Engineering from Sichuan University and China and recently obtained his Ph.D. in Materials Science and Engineering from the University of Washington in the U.S. He is currently working in Apple Inc R&D division as a system hardware engineer focusing on developing the next generation of Apple products.



E. James Davis is Professor Emeritus of Chemical Engineering and Editor-in-Chief Emeritus of the Journal of Aerosol Science. He has been active for many years in the study of elastic and inelastic (Raman) light scattering by microparticles and nanoparticles. This includes a variety of aerosols, crystalline nanoparticles, and biological particles (pollen and bacteria).



Peter J. Pauzauskie received BS degrees in chemical engineering, chemistry, and mathematics from Kansas State U. in 2002, and his PhD in physical chemistry from UC Berkeley in 2007 as an NSF-GRF. He is currently an associate professor of MSE at the University of Washington. He received NSF-CAREER, AFOSR-YIP, and NAE recognition for basic research involving nanoscale optoelectronic materials.



to enhance cooling. For example, materials with surface doping or tetrad clusters.<sup>[53,54]</sup> Similarly, for semiconductor laser cooling applications, unpassivated trap states at the surface of nanomaterials may introduce location-dependent cooling efficiencies and a diffusive driving force if the excited state lifetime is sufficiently long. In this instance, multiscale modeling that accounts for these different effects is required. The resulting source term for cooling can be used to solve for the resulting temperatures with this theoretical framework.

For spheres with radii much smaller than the wavelength of the incident irradiation (that is, for  $x = 2\pi R/\lambda \ll 1$ ) Rayleigh scattering can be used,<sup>[35,47]</sup> which yields [Eq. (4)]

$$\dot{Q} = 3 \cdot \text{Im} \left\{ \frac{m^2 - 1}{m^2 + 2} \right\} \frac{I_0}{R}, \quad (4)$$

where  $m$  is the refractive index of the nanomaterial,  $n_{\text{ref}1}$ , relative to that of the surroundings,  $n_{\text{ref}2}$ , that is,  $m = n_{\text{ref}1}/n_{\text{ref}2}$ ,  $I_0$  is the incident irradiance, and  $R$  is the radius.

It is convenient to write the governing heat transfer partial differential equation in non-dimensional form. For example, in Cartesian coordinates we define the following non-dimensional coordinates and parameters [Eq. (5a)] [Eq. (5b)] [Eq. (5c)] [Eq. (5d)] [Eq. (5e)] [Eq. (5f)]

$$\Theta = \frac{(T - T_\infty)}{T_\infty}, \quad (5a)$$

$$\tau = \frac{\kappa_1 t}{\rho C L_x^2}, \quad (5b)$$

$$\xi = \frac{x}{L_x}, \quad (5c)$$

$$\eta = \frac{y}{L_y}, \quad (5d)$$

$$\zeta = \frac{z}{L_z}, \quad (5e)$$

$$\sigma = \frac{L_x^2}{\kappa_1 T_\infty} \dot{Q} \quad (5f)$$

in which  $L_x$  is the thickness of the object,  $L_y$  is its width,  $L_z$  is its length, and  $T_\infty$  is the temperature of the surroundings far from the nanoparticle. In this case, the governing energy equation reduces to [Eq. (6)]

$$\frac{\partial \Theta}{\partial \tau} = \nabla^2 \Theta + \sigma \quad (6)$$

The heating/cooling of nanoribbons has been explored by Zhang et al.<sup>[55]</sup> using a pump laser to illuminate a CdS nanoribbon suspended over etched trenches in an SiO<sub>2</sub>/Si substrate, and Pant et al.<sup>[56]</sup> determined the temperature of CdS nanoribbon cantilevers by measuring the fundamental acoustic eigenfrequency of the cantilever by means of forward-scattered laser interferometry. In such studies the pump laser beam has

a Gaussian distribution, and for a thin nanoribbon the electric vector for a Gaussian beam can be approximated by<sup>[57]</sup> [Eq. (7)]

$$E(r, z) = \hat{x} E_0 \exp\left(-\frac{r^2}{w_0^2}\right) \exp(-ikz), \quad (7)$$

in which  $\hat{x}$  is the unit vector in the  $x$ -direction,  $E_0$  is the electric field amplitude at  $r=0$ ,  $r$  is the radial distance from the center of the beam, and  $w_0$  is the beam waist radius. Using this relation in Eq. (2), the source function becomes [Eq. (8)]

$$\dot{Q}(r, z) = \frac{4\pi n''}{\lambda_0} I_0 \exp\left(-\frac{2r^2}{w_0^2}\right) \exp(-2k_{\text{im}}z). \quad (8)$$

In many applications in which the laser beam is not sharply focused, for example, in photothermal and photodynamic therapies or photocatalysis,<sup>[58,59]</sup> the incident beam can be treated as a plane wave.

## 2.2 Boundary Conditions

To obtain temperatures from the second order energy equation [Eq. (1)], we must define initial conditions and boundary conditions, which depend on the geometry and other characteristics of the system. For example, high aspect ratio nanowires were held in a single-beam laser trap surrounded by water in the experiments described by Roder et al.<sup>[60]</sup> Their particular experimental system is shown in Figure 2. If we seek the steady state solution, there will be no time dependence—that is,  $\partial T/\partial t = 0$ , or, non-dimensionally  $\partial \Theta/\partial \tau = 0$ —and we are left to define the radial, azimuthal, and axial components. These are  $r$ ,  $\theta$  and  $z$  dimensionally, or  $\xi$ ,  $\phi$ , and  $\zeta$ , non-dimensionally, respectively.

The heat flux from the ends of the nanowire to the upper and lower coverslips of the trap were assumed to be described by Fourier's law of heat conduction, which states that the flux of energy in a material is proportional to the negative temper-

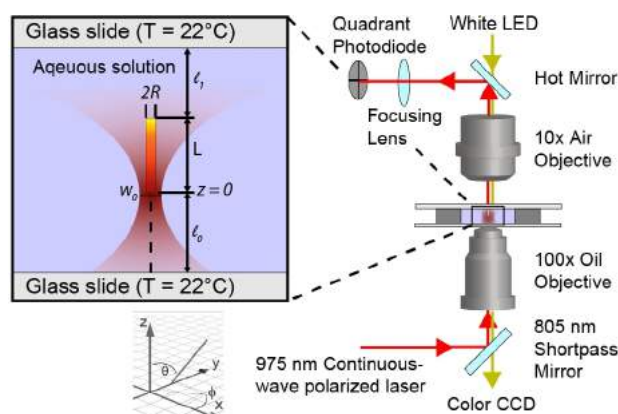


**Figure 2.** An example optical trapping instrument showing the optical trapping and heating of a nanowire, and the coordinate system for heat transport modeling. Figure reproduced with permission from reference [61] copyright the American Chemical Society.



ature gradient times the thermal conductivity. In the non-dimensional form, this simplifies to [Eq. (9)]

$$\left(\frac{\partial \Theta}{\partial \xi}\right)_{\xi=0} = \frac{\kappa_2 L}{\kappa_1 L_0} \Theta_{\xi=0}, \quad \left(\frac{\partial \Theta}{\partial \xi}\right)_{\xi=1} = \frac{\kappa_2 L}{\kappa_1 L_1} \Theta_{\xi=1}, \quad (9)$$

in which  $L_0$  and  $L_1$  represent the distances between the rod ends and the lower and upper surfaces of the trap, respectively,  $\kappa_1$  and  $\kappa_2$  represent the thermal conductivity of the nanowire and the medium, respectively.

Radially, it is convenient to define the Biot number,  $Bi = hL_c/\kappa_1$ , which is the ratio of heat transfer conducted away from a material to the heat transferred within a material. Here  $L_c$  is the characteristic length of the material. We use this to define the radial boundary condition, [Eq. (10)]

$$\left(\frac{\partial \Theta}{\partial \xi}\right)_{\xi=1} = -Bi_\xi \Theta_{\xi=1}, \quad (10)$$

where the Biot number for the radial direction is related to the appropriate heat transfer coefficient,  $h$ , for heat transfer to the surrounding medium. The heat transfer coefficient for convective and conductive heat transfer is usually written in terms of the dimensionless Nusselt number,  $Nu$ , defined by  $Nu = hL_c/\kappa_2$ . For cylinders in a stagnant fluid experimental measurements<sup>[61]</sup> yield  $Nu = hD/\kappa_2 = 0.32$ , in which  $D$  is the diameter. For spheres in a stagnant fluid  $Nu = hD/\kappa_2 = 2$ , and for spheres, oblate spheroids, cylinders and other particles in flowing fluids there exists a large literature on convective heat transfer.

If the nanowire is initially at the temperature of the trap,  $T_\infty$  then, it remains to specify the boundary conditions in the angular direction, and that depends on the structure of the source function. For a uniform, unpolarized laser source or when the source is not a function of  $\phi$ , there is no  $\phi$  dependence to the solution. Roder et al.<sup>[60]</sup> illuminated the nanowire in the  $z$ -direction with an unpolarized laser, so there was no heat flow in the  $\phi$  direction, that is, [Eq. (11)]

$$\left(\frac{\partial \Theta}{\partial \phi}\right)_{\phi=0,\pi} = 0. \quad (11)$$

In the experiments of Zhang et al. and Pant et al. the nanoribbons were mounted in a vacuum chamber, so there was no conductive or convective heat transfer to the surroundings. In this event only radiative heat transfer to the surroundings and conductive heat transfer to the substrate occur. If the surface temperature,  $T_s$ , and that of the vacuum chamber,  $T_\infty$ , are not greatly different, the heat flux from the surface,  $q_s$ , may be approximated by linearizing the Stefan–Boltzmann equation as follows [Eq. (12)]

$$q_s = \epsilon \sigma_{SB} (T_s^4 - T_\infty^4) \simeq \epsilon \sigma_{SB} 4T_\infty^3 (T_s - T_\infty), \quad (12)$$

in which  $\epsilon$  is the emissivity of the nanoribbon,  $\sigma_{SB}$  is the Stefan–Boltzmann constant. Consequently, the dimensionless boundary condition at the surface becomes [Eq. (13)]

$$\left(\frac{\partial \Theta}{\partial \xi}\right)_s = Bi_s \Theta_s, \quad (13)$$

where we have assumed that the heat transfer is in the  $z$ -direction, and  $H$  is the thickness of the nanoribbon. In this case the Biot number is defined by [Eq. (14)]

$$Bi_s = \frac{H}{\kappa_1} \epsilon \sigma_{SB} 4T_\infty^3. \quad (14)$$

Frequently the Biot number for nanomaterials is very small, which corresponds to a nearly zero heat flux from a surface and a uniform internal temperature. While this linearized approximation produces an error of 38% when is 100 K above ambient conditions, the rate of radiative heat loss is significantly less than conductive or convective losses, and it is an appropriate approximation. When the difference between  $T_s$  and  $T_\infty$  is greater than 10 K (with = 298 K), the error associated with this approximation grows beyond 5%. Because radiative heat loss is often significantly less than the conductive or convective heat losses, this linearization is an appropriate approximation. At high temperatures, Crane et al. overcome this issue by introducing an iterative term in the boundary condition,  $Bi_s = A \frac{H}{\kappa_1} \epsilon \sigma_{SB} T_\infty^3$ , where  $A$  is defined by<sup>[62]</sup> [Eq. (15)]

$$A = T_s^3 + T_s^2 T_\infty + T_s T_\infty^2 + T_\infty^3 \quad (15)$$

Allen et al. considered the case of an absorbing liquid microsphere trapped in a gaseous environment with an electrodynamic balance.<sup>[63]</sup> Unlike trapping a solid nanowire in a liquid, when the liquid microsphere absorbs energy, it evaporates. To capture this effect, Allen modified the heat transfer coefficient to include the energy lost to the phase transformation as [Eq. (16)]

$$h = \frac{\lambda_{vap} D_{ij} M_i \rho_i^0}{a R^2 T_\infty^3} \quad (16)$$

where  $\lambda_{vap}$ ,  $D_{ij}$ ,  $M_i$  and  $\rho_i^0$  are the heat of vaporization, the diffusion coefficient, the molecular weight, and density of the liquid phase, and  $R$  is the gas constant. Including these terms is essential for applications with phase changes, such as sono-photoacoustic contrast agents, tumor ablation, or photocatalysis.<sup>[2, 7, 62, 64]</sup>

### 2.3 Solution of the Energy Equation

The classical approach to solving the energy equation is application of the product method. We illustrate this by considering the photothermal heating of CdS nanoribbons (CSNR) explored by Smith et al.<sup>[65]</sup> Figure 3 presents a scanning electron micrograph and a transmission electron micrograph of CSNRs.

The dimensionless energy equation becomes [Eq. (17)]

$$\frac{\partial \Theta}{\partial \tau} = \frac{\partial^2 \Theta}{\partial \xi^2} + a^2 \frac{\partial^2 \Theta}{\partial \eta^2} + b^2 \frac{\partial^2 \Theta}{\partial \xi^2} + \sigma(\xi, \eta, \xi), \quad (17)$$

$$A = T_s^3 + T_s^2 T_\infty + T_s T_\infty^2 + T_\infty^3$$

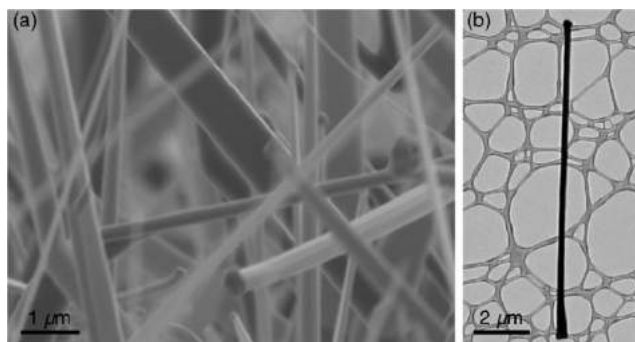


**Figure 3.** CdS nanoribbons. (a) A scanning electron micrograph of CSNRs on a silicon wafer. (b) A low-magnification transmission electron micrograph of as single CSNR. Figure reproduced with permission from reference [65] copyright the International Society for Optics and Photonics.

in which [Eq. (18a)] [Eq. (18b)] [Eq. (18c)]

$$a = \frac{L_x}{L_y}, \quad (18a)$$

$$b = \frac{L_x}{L_z}, \quad (18b)$$

$$\sigma = \frac{L_x^2}{\kappa_1 T_\infty} \dot{Q}. \quad (18c)$$

Here  $2L_x$  is the thickness of the thin nanoribbon,  $2L_y$  is the width, and  $L_z$  is the length as shown in Figure 4a. The discrete dipole approximation was used to determine the source function,  $\dot{Q}$ , and Figure 4b shows the normalized electric field. We have assumed that the source function is independent of time, but if a pulsed laser is used, we must take that into account in the source function. Figure 4c shows that the average of the normalized electric field increases to a maximum value at the upper end of the object.

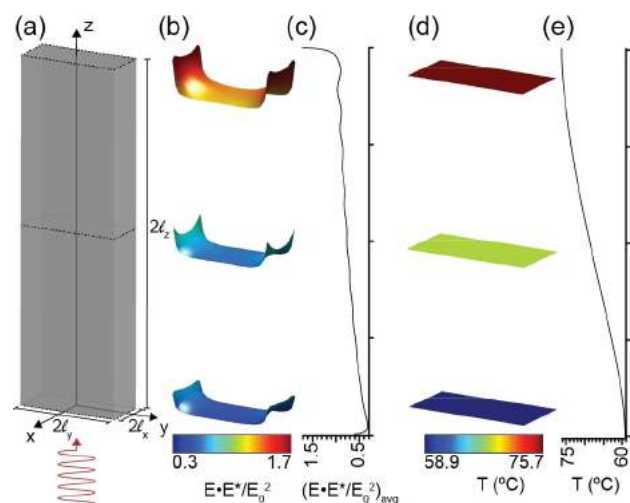


**Figure 4.** Photothermal heating of CdS nanoribbons, including the coordinate system (a), a cross section and average axial field of the normalized electric field source term (b and c) and the steady state temperature profile (d and e). Figure reproduced with permission from reference [65] copyright the International Society for Optics and Photonics.

The solution has the form [Eq. (19)]

$$\Theta(\xi, \eta, \zeta, \tau) = \sum_{l=1}^{\infty} \sum_{m=1}^{\infty} \sum_{n=1}^{\infty} A_{lmn}(\tau) X_l(\xi) Y_m(\eta) Z_n(\zeta), \quad (19)$$

where  $X_l(\xi)$ ,  $Y_m(\eta)$ , and  $Z_n(\zeta)$  are orthonormal eigenfunctions given by Smith et al., and the coefficients  $A_{lmn}(\tau)$  are related to the source function by [Eq. (20)]

$$A_{lmn}(\tau) = \frac{[1 - \exp(-\alpha_{lmn}^2 \tau)]}{\alpha_{lmn}^2} \int_0^1 \int_0^1 \int_0^1 \sigma(\xi', \eta', \zeta') X_l(\xi') \cdot Y_m(\eta') Z_n(\zeta') d\xi' d\eta' d\zeta' \quad (20)$$

where the prime indicates dummy variables of integration and  $\alpha_{lmn}^2$  is related to the eigenvalues  $\beta_l$ ,  $\gamma_m$ ,  $\delta_n$  corresponding to the eigenfunctions  $X_l(\xi)$ ,  $Y_m(\eta)$ , and  $Z_n(\zeta)$ , respectively, and is defined by [Eq. (21)]

$$\alpha_{lmn}^2 = \beta_l^2 + a^2 \gamma_m^2 + b^2 \delta_n^2. \quad (21)$$

The steady state solution is obtained by taking the limit  $\tau \rightarrow \infty$  in Eq. (20). We note that the source function here is independent of time but can be appropriately modified for pulsed heating.

The temperature distribution computed using these results is shown in Figure 4e. The temperature is fairly uniform in the x-y plane, but decreases significantly in the z-direction as shown by the average temperatures in the x-y planes presented in Figure 4d.

This general approach was applied to analyze pulsed heating of a cone-shaped atom probe tomography specimens by Roder et al.<sup>[27]</sup> The configuration analyzed by them is shown in Figure 5, and some results of the analysis are shown in Figure 6. Figure 6a presents the axial temperature distribution following a laser pulse for various taper angles,  $\theta$ . Counterin-

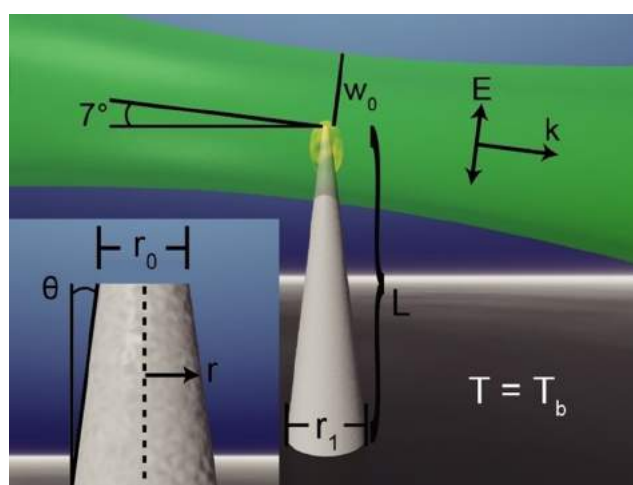


**Figure 5.** The configuration of a tapered atom probe tomography specimen irradiated by a focused pulsed laser. Figure reproduced with permission from reference [27] copyright American Chemical Society.

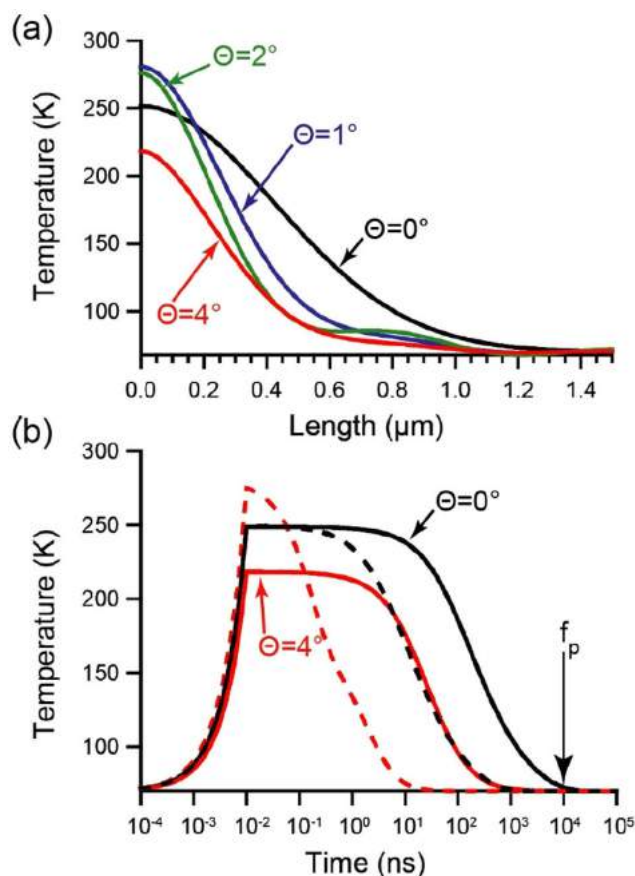


**Figure 6.** Time-dependent heating of silicon nanostructures. (a) The axial temperature distribution in tapered (0°, 1°, 2°, and 4°) amorphous silicon nanowires immediately after a 0.23 W laser pulse. (b) Corresponding temperatures of the 0° and 4° tapered nanowire tips with characteristic cooling time,  $f_p$ . Figure reproduced with permission from Reference [27], copyright American Chemical Society.

tuitively, increasing the taper angle can lead to an increase in the maximum temperature of the specimen.

A useful metric to verify experimental observations of photothermal heating or cooling is to measure the time-dependent change in temperature after the heating or cooling laser is turned off. These data can be used to distinguish optical heating or cooling from other photophysical phenomena by comparing the time scales of different mechanisms. To aid in this process, we have calculated the nondimensional time,  $\tau$ , for a nonequilibrium sphere with radius,  $r$ , to return within 99% of room temperature as a function of the heat transfer coefficient,  $h$ , shown in Figure 7. The approximate heat transfer coefficient,  $h$ , can be calculated from Table 1. By then finding the value  $\tau$  of using Figure 7, the time can be estimated with Eq. (22)

$$t = \frac{a^2 \rho C}{\kappa_1} \frac{1}{\tau} \quad (22)$$

For 1 μm radii spheres of CdS, YAG, and YLF dispersed in water ( $=0.059 \text{ W m K}^{-1}$ ), the cooling time scale is  $3 \times 10^{-8}$ ,  $4 \times 10^{-7}$ , and  $1 \times 10^{-6}$  s, respectively. If the measured cooling

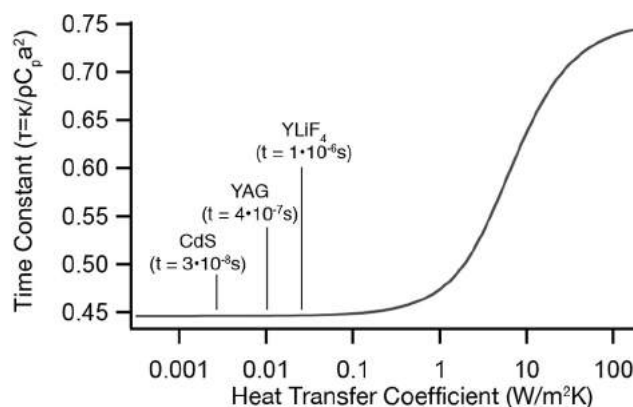


**Figure 7.** Unsteady state heat transport for a sphere with different heat transfer coefficients. The inset shows the low heat transfer coefficient region and the predicted time to reach 99% of the ambient temperature.

time scale is more than an order of magnitude different than these values, different physical mechanisms should be used to explain the observations.

### 3. Photothermal Cooling

#### 3.1 Introduction to Laser Cooling

In contrast to laser heating, it is also possible to use laser radiation to refrigerate nanoscale materials. There are two primary mechanisms used to observe the laser cooling of matter. The most well-known laser cooling mechanism based on the Doppler cooling of dilute gases, which was awarded the Nobel Prize in physics in 1997.<sup>[66]</sup> Through interaction with counter-propagating laser beams, the velocity of the atoms in vacuum can be slowed down, which results in a temperature of 1 μK or below. In order to achieve such a low temperature, a low atom density ( $< 10^{13} \text{ cm}^{-3}$ ) in high vacuum is usually required to minimize the atomic interactions. Doppler cooling enables the study of fundamental physics, such as Bose–Einstein condensa-

Table 1. Nusselt numbers for various geometries.			
	Characteristic Length ( $L_c$ ) <sup>[a]</sup>	Stagnant Limit <sup>[b]</sup>	Nusselt number with natural convection <sup>[c]</sup>
Sphere	Diameter	2	$2 + 0.6 Re^{1/2} Pr^{1/3}$
Horizontal cylinder	Diameter	0.32	$0.32 + 0.43 Re^{0.52}$
Vertical cylinder	Height	0.68	$0.68 + 0.6 Re^{1/2} Pr^{1/3} (1 + (0.482/Pr))^{-9/16}$

[a] The heat transfer coefficient is equal to  $Nu \kappa_2 / L_c + 4\epsilon\sigma T_\infty^3$ . [b] The stagnant limit is valid for low Reynolds numbers, where  $Re = \nu \rho L_c / \mu$ , which encompasses almost all scenarios. Here,  $\nu$ ,  $\rho$ ,  $L_c$ , and  $\mu$  are the fluid viscosity, density, characteristic length, and viscosity. [c] When convection becomes a significant heat loss, the full Nusselt number correlation should be used. The convective effects are incorporated through the Grashof number,  $Gr = g\beta\Delta T L^3 / \mu^2$ , and the Prandtl number,  $Pr = \mu \rho C_p / \kappa$ , where  $g$ ,  $\beta$ ,  $\rho$ , and  $C_p$  are the acceleration due to gravity, the thermal expansion coefficient, density, and heat capacity of the medium evaluated at the film temperature.  $\Delta T$  is the difference in temperature between the particle surface and the bulk solvent temperature. Additional correlations can be found in reference [45].



tion and atom clocks.<sup>[67]</sup> However, the application of Bose-Einstein condensates in condensed solids is limited.

In contrast to Doppler cooling in vacuum, the primary approach for the laser cooling of condensed matter is based on anti-Stokes fluorescence. In 1929, Pringsheim proposed that the vaporized sodium atoms could be excited at certain wavelength photon and then emit a mean shorter wavelength photon, which is called anti-Stokes fluorescence. The energy difference between the excited photon and emitted photon will extract heat from the material and cause net cooling.<sup>[68]</sup> This cooling mechanism was theoretically proven to be consistent with the second law of thermodynamics by Landau in 1946 through quantifying the overall change in entropy between excitation and anti-Stokes/fluorescence photons.<sup>[69]</sup> In 1950, Kastler proposed to dope rare earth (RE) ions in transparent crystals, which could provide high quantum efficiency for anti-Stokes fluorescence.<sup>[70]</sup> This is due to the unique 4f shell of RE ions suppressing the non-radiative relaxation process. During the anti-Stokes fluorescence cooling an energy difference of approximately  $k_bT$  separates the absorbed photon from the emitted photon, requiring a narrow spectra line excitation source to achieve laser cooling. Such narrow sources were not achieved until the development of the laser in the 1960s. In 1963, Kushida reported the first demonstration of reduced heating of a solid using with laser light.<sup>[72]</sup> In this work, a 1064 nm laser was used to excite  $\text{Nd}^{3+}$  ions doped within  $\text{Y}_3\text{Al}_5\text{O}_{12}$  (YAG) crystals which were observed to emit anti-Stokes fluorescence at 946 nm resulting in a reduction of heating of the YAG gain crystal. However, the overall net cooling of laser refrigeration through anti-Stokes fluorescence was not achieved until 1995 when Epstein and co-workers demonstrated a 0.3 K net cooling using a continuous-wave NIR laser at a wavelength of 1030 nm to refrigerate amorphous ZBLAN glass doped with  $\text{Yb}^{3+}$  ions.<sup>[72]</sup> One limitation of using amorphous materials for solid-state laser refrigeration is that the crystal-field levels of rare-earth ions in glasses exhibit significant inhomogeneous broadening, which lowers the overall absorption when using narrow laser excitation wavelengths. This challenge was overcome in the early 2000's when crystalline host materials with well-defined crystal field energies began to be explored. So far, a number of materials have exhibited laser cooling with  $\text{Yb}^{3+}$  ions, including ZBLAN, CNBZn, BIG,  $\text{KGd}(\text{WO})_4$ ,  $\text{KY}(\text{WO})_4$ , YAG,  $\text{Y}_2\text{SiO}_5$ ,  $\text{KPB}_2\text{Cl}_5$ ,  $\text{BaY}_2\text{F}_8$ , YLF,  $\text{NaYF}_4$ .<sup>[72–80]</sup> More recently both CdS and perovskite materials have been reported to refrigerate through a similar anti-Stokes fluorescence process by the Xiong lab<sup>[55,81]</sup> although the laser refrigeration of these materials has yet to be reproduced by other laboratories.

In 2015, a record low temperature for laser cooling was demonstrated by the Sheikh-Bahae laboratory at the University of New Mexico. In particular, they reported that  $\text{Yb}^{3+}:\text{YLF}$  bulk crystals can be cooled in vacuum to 91 K from room temperature with tuning the excitation of the crystal to  $\text{Yb}^{3+}$   $\text{E}_4\text{--E}_5$  resonance at 1020 nm, shown in Figure 8. The energy levels of  $\text{Yb}^{3+}$  are shown in Figure 9b.<sup>[82]</sup>

To date, the best materials for solid-state laser cooling are fluoride crystals doped with rare-earth (RE) ions that absorb ex-

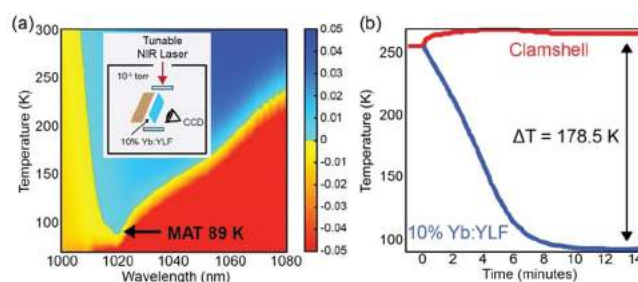


**Figure 8.** (a) Blue regions denote cooling, and red regions denote heating. The minimum achievable temperature (MAT) of 89 K is highlighted. (Inset) Illustration of the cooling cavity, which enables multiple passes of the cooling laser through the crystal. (b) The crystal temperature (blue) reaches 91 K after  $\approx 12$  minutes of pumping while the clamshell temperature is maintained at  $\approx 265$  K. Figure reproduced with permission from reference [82] copyright Nature Publishing Group.

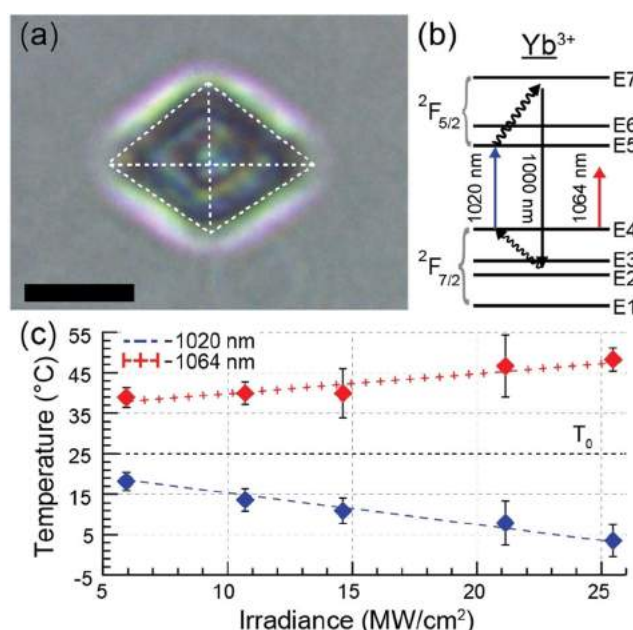


**Figure 9.** Laser refrigeration of optically trapped YLF microcrystals. (A) Optical micrograph of an optically-trapped YLF crystal. (Scale bar, 3  $\mu\text{m}$ .) (B) Crystal-field energy level configuration of  $\text{Yb}^{3+}$  dopant ions and used cooling scheme. (C) Extracted temperature of optically trapped particles in  $\text{D}_2\text{O}$  as determined using CBM theory.  $\text{Yb}^{3+}$ -doped YLF particles are shown to cool when trapping wavelength is resonant with the  $\text{E}_4\text{--E}_5$  transition ( $\lambda = 1,020$  nm) but heat when the trapping wavelength is below the transition ( $\lambda = 1064$  nm). Figure reproduced with permission from reference [19] copyright National Academy of Sciences.

citation photons with an energy,  $h\nu$ .  $\text{Yb}^{3+}$  ions have a ground state electron configuration with 13 electrons in 4f orbitals. In the cooling cycle, absorption of a low entropy laser excites a ground state electron from level  $\text{E}_4$  to the lowest energy excited state  $\text{E}_5$ . Spin-orbit-coupling leads to long ( $\tau \approx 1.8$  ms) excited state lifetimes for  $\text{Yb}^{3+}$  ions, which provides sufficient time for the excited hole to couple with an optical phonon from the surrounding crystal lattice. The effect of this coupling is to thermalize holes to higher energy states within the 4f energy levels. Subsequent radiation from these higher energy states



with fluorescence photon energy  $h\nu_f$ , contains the energy from the absorbed phonons. Therefore, the simplified cooling efficiency  $\eta_c$  can be expressed as [Eq. (23)]

$$\eta_c = \frac{h\nu_f - h\nu}{h\nu} = \frac{\lambda}{\lambda_f} - 1 \quad (23)$$

in which  $\lambda$  is the excitation wavelength and  $\lambda_f$  is the mean fluorescence wavelength. For the excited cooling ions, there is a fraction of energy that may relax non-radiatively (thermalize) to generate heat. Following radiative relaxation, there may also be reabsorption of the fluorescence photons by ground state  $\text{Yb}^{3+}$  ions, which ultimately decreases the overall cooling efficiency. In addition, non-radiative relaxation from transition metal impurities within the host material can also absorb pump photons to produce parasitic background heating. The combination of all the factors described above defines the laser cooling efficiency as [Eq. (24)]

$$\eta_c = \frac{\eta_{\text{esc}} W_{\text{rad}}}{\eta_{\text{esc}} W_{\text{rad}} + W_{\text{nr}}} \frac{\alpha_r}{\alpha_r + \alpha_b} \frac{\lambda}{\lambda_f} - 1 \quad (24)$$

where  $W_{\text{rad}}$  and  $W_{\text{nr}}$  are the radiative and nonradiative relaxation rate of the excited cooling ions, respectively,  $\eta_{\text{esc}}$  is the escaping coefficient,  $\alpha_b$  is the background absorption coefficient, and  $\alpha_r$  is the material absorption coefficient.

Another method to evaluate the material's cooling performance is to compare the entropy of the incident and fluorescence light.<sup>[69]</sup> Ruan et al. have shown that the entropy flow rate,  $\dot{S}$ , per unit power,  $P$ , under a narrow-band approximation can be used, which is expressed as [Eq. (25)],<sup>[83]</sup>

$$\frac{\dot{S}}{P} = \frac{k_B}{\hbar\omega_0} \frac{(1 + \bar{n}) \ln(1 + \bar{n}) - \bar{n} \ln \bar{n}}{\bar{n}} \quad (25)$$

where  $k_B$  and  $\hbar$  are the Boltzmann and Planck's constants,  $\omega_0$  is the central frequency, and  $\bar{n}$  is the average distribution function given by [Eq. (26)]

$$\bar{n} = \frac{P}{A\Delta\omega\pi\sin^2\delta} \frac{4\pi^3 c^2}{\hbar\omega_0^3} \quad (26)$$

Here,  $P$  is the power,  $A$  is the emission area,  $\Delta\omega$  is the spectral bandwidth,  $\delta$  is the emission divergence angle, and  $c$  is the speed of light.

Based on the first law of thermodynamics, the laser cooling process can be explained as [Eq. (27)]

$$P_{\text{out}} = P_{\text{in}} + Q_c \quad (27)$$

$P_{\text{out}}$  and  $P_{\text{in}}$  refer to the fluorescence and excitation light energy, respectively, and  $Q_c$  is the cooling load. The second law of thermodynamics can be written as [Eq. (28)],

$$\dot{S}_{\text{out}} \geq \dot{S}_{\text{in}} + \dot{S}_c \quad (28)$$

where  $\dot{S}_{\text{out}}$ ,  $\dot{S}_{\text{in}}$ ,  $\dot{S}_c$  are entropy flow rates for output emission, absorbed irradiation, and thermal load. The laser cooling efficiency is then defined as [Eq. (29)],

$$\eta = \frac{Q_c}{P_{\text{in}}} \quad (29)$$

and the Carnot limit can be obtained [Eq. (30)]

$$\eta_{\text{Car}} = \frac{[(\dot{S}/P)_{\text{out}} - (\dot{S}/P)_{\text{in}}]T}{1 - (\dot{S}/P)_{\text{out}}T} \quad (30)$$

Increasing  $(\dot{S}/P)_{\text{out}}$  and decreasing  $(\dot{S}/P)_{\text{in}}$  improve the ultimate thermodynamic limit.

Laser cooling, as solid-state refrigerators, enables a wide range of practical applications which require strict size, mass, power, and stability, such as space-based or airborne deployment. Compared with bulky mechanical cryocoolers that vibrate and must be in physical contact with the cooling medium, laser cooling has no moving parts, is compact, and conducts heat from the solid to environment by exclusively through fluorescence without the need for physical contact. Solid state laser refrigeration may also lead to cooling to temperatures below 100 K, beyond what is possible with thermoelectric coolers (175 K). This opens up applications for solid state laser refrigeration in cooling laser reference cavities used in the detection of gravitational waves, gamma-ray detectors, and high-temperature superconductors.<sup>[82]</sup>

### 3.2 Laser Cooling with Nanomaterials

Despite impressive progress in the refrigeration of bulk crystals in vacuum, an open question has remained regarding whether it is possible to refrigerate nanometer scale YLF materials or to refrigerate in condensed solvents like water, which are relevant for chemical reactions or can act as working fluids in heat exchangers. There is one report of condensed phase laser refrigeration in the literature using the optical excitation of rhodamine dyes,<sup>[84]</sup> though to the best of the authors' knowledge this report remains to be reproduced. More recent experiments using single-beam laser trapping have been undertaken to demonstrate the laser-refrigeration of nanoscale YLF materials in condensed media, including liquid water, physiological electrolytes, and  $\text{D}_2\text{O}$  as shown in Figure 9. The cold Brownian motion (CBM) of an individual  $\text{Yb}^{3+}$ :YLF crystal in an optical trap is quantified by analyzing forward scattered laser radiation that is directed to a quadrant photodiode. Figure 9 also shows a control experiment using a trapping laser wavelength of 1064 nm, which has a photon energy that is insufficient to pump E4-E5 crystal field transitions within  $\text{Yb}^{3+}$  ions. This is the first demonstration of cold Brownian motion since Einstein's seminal work on Brownian motion published in 1905. The ability to optically generate local cold regions around individual nanocrystals promises to enable precise optical temperature control within integrated electronic, photonic, and microfluidic circuits, thermal modulation of basic biomolecular processes, investigation of the gravitational reduction of quantum

states, and the search for non-Newtonian gravity at small scales.<sup>[85]</sup> Most recently, optical tweezers have been used in vacuo to trap and refrigerate individual  $\text{Yb}^{3+}$ :YLF nanocrystals prepared through the ball-milling of bulk crystals.<sup>[86]</sup> A levitated  $\text{Yb}^{3+}$ :YLF nanocrystal was refrigerated through anti-Stokes fluorescence to a minimum temperature of 130 K in vacuum in which the temperature was determined through a ratiometric Boltzmann analysis of collected fluorescence spectra. This enables cooling of both the center of mass and internal temperature in vacuum, which is promising in study of macroscopic quantum mechanics, precision measurements of forces, and non-equilibrium thermodynamics.

Nanostructures for laser cooling can be prepared through top down methods such as the milling of bulk crystals, or through bottom-up approaches based on chemical synthesis. The Czochralski synthesis of bulk crystals has stringent requirements for the chemical purity of synthetic precursors and also requires expensive growth facilities to achieve high purity and minimal defects to maximize cooling efficiency. Czochralski growth also requires long time scales (weeks to months) and large amounts of reagents ( $\approx 100$  g). In contrast to Czochralski growth, the hydrothermal synthesis of nanocrystals for laser cooling employs low-cost autoclaves, requires small amounts of high-purity chemical reagents (milligrams), and modest amounts of time for reactions to complete (hours to days). In this way, the laser cooling of nanostructures prepared through hydrothermal synthesis can be applied for sample testing to optimize the host material and dopant selection to help inform Czochralski single crystal growth. In addition, hydrothermal growth has the potential to produce new phases that cannot be grown in bulk, such as the hexagonal ( $\beta$ ) phase of  $\text{NaYF}_4$  materials. As a widely studied upconverting material,  $\text{NaYF}_4$  materials have been used in a range of applications, including bioimaging, drug delivery, photothermal therapy, optical information storage, solar cells, and volumetric 3D displays.<sup>[87–89]</sup> However, the traditional Czochralski method causes bulk  $\beta$ - $\text{NaYF}_4$  crystals to crack upon cooling due to anisotropic thermal expansion coefficients. Zhou et al. recently demonstrated the laser cooling of biocompatible  $\beta$ - $\text{NaYF}_4$  nanowires in  $\text{D}_2\text{O}$  using single-beam optical tweezers.<sup>[19]</sup> This was the first demonstration of laser cooling of  $\beta$ - $\text{NaYF}_4$ , which is predicted to reach lower temperatures than YLF due to its small crystal field splitting energy.

## 4. Conclusions

This Focus Review provides a concise overview of several recent advances in the field of photothermal heating and cooling of inorganic nanostructures, including theoretical modeling and experimental measurements using both continuous and pulsed laser excitation. Nanoscale photothermal heating and cooling of inorganic nanostructures has myriad applications in both basic and applied research, and the field is constantly evolving based on advances in chemical synthesis, theoretical modelling, and experimental characterization.

To drive photothermal heat management at nanometer length scales, future research should target the experimental

evaluation and theoretical modeling of nanoscale heat transport effects, such as size-dependent thermal conductivity<sup>[25,26]</sup> or thermal boundary resistances. The study and incorporation of these effects into Fourier's law are essential to enable accurate nanoscale heat transport engineering.<sup>[90]</sup> For example, the development of the diffuse phonon mismatch model,<sup>[32,91]</sup> the calculation of thermal boundary resistances from ab initio phonon dispersions,<sup>[92]</sup> and distinguishing electron-phonon from phonon-phonon conductances<sup>[93]</sup> will extend the application of Fourier's law. Much like the compilation of thermal conductivities and application of dimensionless numbers have driven analytical heat transport in the 20th century,<sup>[45]</sup> the compilation of interfacial conductance constants<sup>[93]</sup> and rules for their application will be needed in the 21<sup>st</sup> century. This will necessarily include the increased prominence of computational materials science.<sup>[39,91]</sup> Experimentally, the development of new optical tools to study heat transport are paramount to the goal of engineering heat management at the nanoscale.<sup>[31,46,94–96]</sup> To further improve the laser cooling efficiency of nanocrystals, several methods could potentially be applied. First, surface coatings of inert shells on nanocrystals may reduce parasitic multiphonon relaxation and surface quenching. Dipole coupling of the cooling ions with molecular groups attached to the surface of the nanocrystal followed by subsequent nonradiative thermalization causes parasitic heating of the nanostructure, which limits cooling. The addition of an inert shell could minimize the energy transfer, which would result in an improvement of the quantum efficiency and cooling efficiency. Mitigating dipole coupling with molecular species could also be accomplished by chemically modifying the distribution of dopants throughout the nanomaterial. Distributing ions throughout the lattice has the added benefit of reducing energy migration, which can act as a nonradiative recombination mechanism. As an example, Liu et al. have reported that  $\text{KYb}_2\text{F}_7$  with a unique orthorhombic crystal structure can minimize energy migration between  $\text{Yb}^{3+}$  ions with the tetrad clusters.<sup>[54]</sup> The 2%  $\text{Er}^{3+}$  doped  $\text{KYb}_2\text{F}_7$  shows 8 times higher intensity than previously reported. This super-enhanced upconversion structure could potentially be used in laser cooling. Second, different host materials should be investigated for laser cooling applications. In particular, host materials that have demonstrated high efficiency upconversion and low phonon energies should be targeted. Third, alternative pumping schemes and emission methods may increase the possible cooling load. For example, pump-pulse schemes can cause collective emission from ions with shorter lifetimes, known as superradiance,<sup>[97]</sup> reducing the requirement for low-phonon hosts and opening the door to nanocrystal-based laser cooling.<sup>[98]</sup> Fourth, hydrothermal synthesis can make large amounts of high purity and quality nanocrystals for laser cooling application, allowing rapid combinatorial evaluation of materials. An additional advantage of laser cooling with nanocrystals is the ability to couple nanocrystal emission with cavities to extract heat more efficiently.<sup>[99,100]</sup> The development of composite materials for solid state laser refrigeration also is a promising future research direction with the potential to enable the manufacturing of low-cost, safe, and complex three-dimensional

structures for use in a range of complex laser refrigeration applications.

## Acknowledgements

PJP and MJC gratefully acknowledge support from a NSF-CAREER Award (#1555007), the MURI:MARBLE project under the auspices of the AFOSR (#FA9550-16-1-0362), and the US Department of Energy's Pacific Northwest National Laboratory (PNNL), and the PNNL's Materials Synthesis and Simulation Across Scales (MS3) Initiative, a Laboratory Directed Research and Development (LDRD) program at the PNNL. M.J.C. gratefully acknowledges support from the Department of Defense through a National Defense Science and Engineering Graduate Fellowship (NDSEG) program.

## Conflict of interest

The authors declare no conflict of interest.

**Keywords:** anti-stokes • cold Brownian motion • heat transfer • laser cooling • photothermal heating

- [1] J. T. Robinson, S. M. Tabakman, Y. Liang, H. Wang, H. Sanchez Casalogue, D. Vinh, H. Dai, *J. Am. Chem. Soc.* **2011**, *133*, 6825–6831.
- [2] E. C. Dreaden, A. M. Alkilany, X. Huang, C. J. Murphy, M. A. El-Sayed, *Chem. Soc. Rev.* **2012**, *41*, 2740–2779.
- [3] P. K. Jain, X. Huang, I. H. El-Sayed, M. A. El-Sayed, *Acc. Chem. Res.* **2008**, *41*, 1578–1586.
- [4] D. Rings, R. Schachoff, M. Selmke, F. Cichos, K. Kroy, *Phys. Rev. Lett.* **2010**, *105*, 090604.
- [5] G. González-Rubio, P. Díaz-Núñez, A. Rivera, A. Prada, G. Tardajos, J. González-Izquierdo, L. Bañares, P. Lombart, L. G. Macdowell, M. A. Palafox, L. M. Liz-Marzán, O. Peña-Rodríguez, A. Guerrero-Martínez, *Science* **2017**, *358*, 640–644.
- [6] I. L. Violi, J. Gargiulo, C. von Bilderling, E. Cortés, F. D. Stefani, *Nano Lett.* **2016**, *16*, 6529–6533.
- [7] D. S. Li, S. J. Yoon, I. Pelivanov, M. Frenz, M. O'Donnell, L. D. Pozzo, *Nano Lett.* **2017**, *17*, 6184–6194.
- [8] L. Lin, X. Peng, Z. Mao, W. Li, M. N. Yogeesh, B. B. Rajeeva, E. P. Perillo, A. K. Dunn, D. Akinwande, Y. Zheng, *Nano Lett.* **2016**, *16*, 701–708.
- [9] J. Gargiulo, I. L. Violi, S. Cerrota, L. Chvátal, E. Cortés, E. M. Perassi, F. Diaz, P. Zemánek, F. D. Stefani, *ACS Nano* **2017**, *11*, 9678–9688.
- [10] M. J. Crane, P. J. Pauzauskie, *J. Mater. Sci. Technol.* **2015**, *31*, 523–532.
- [11] X.-M. Chen, J. Mao, Y.-Z. Zhou, J. Yang, X.-W. Du, S.-Z. Qiao, *J. Mater. Chem. A* **2016**, *4*, 379–383.
- [12] J. Yeo, S. Hong, G. Kim, H. Lee, Y. D. Suh, I. Park, C. P. Grigoropoulos, S. H. Ko, *ACS Nano* **2015**, *9*, 6059–6068.
- [13] D. J. Hwang, S.-G. Ryu, C. P. Grigoropoulos, *Nanotechnology* **2011**, *22*, 385303.
- [14] D. J. Hwang, S. Ryu, E. Kim, C. P. Grigoropoulos, C. Carraro, *Appl. Phys. Lett.* **2011**, *99*, 123109.
- [15] A. P. Bregulla, H. Yang, F. Cichos, *ACS Nano* **2014**, *8*, 6542–6550.
- [16] D. Smith, C. Woods, A. Seddon, H. Hoerber, *Phys. Chem. Chem. Phys.* **2014**, *16*, 5221–5228.
- [17] M. Iwaki, A. H. Iwane, K. Ikezaki, T. Yanagida, *Nano Lett.* **2015**, *15*, 2456–2461.
- [18] P. B. Roder, B. E. Smith, X. Zhou, M. J. Crane, P. J. Pauzauskie, *Proc. Natl. Acad. Sci. USA* **2015**, *112*, 15024–15029.
- [19] X. Zhou, B. E. Smith, P. B. Roder, P. J. Pauzauskie, *Adv. Mater.* **2016**, *28*, 8658–8662.
- [20] J. D. Jackson, *Classical Electrodynamics Third Edition*, Wiley, Hoboken, **1998**.
- [21] G. Baffou, *Thermoplasmonics: Heating Metal Nanoparticles Using Light*, Cambridge University Press, Cambridge, **2017**.
- [22] S. Merabia, S. Shenogin, L. Joly, P. Keblinski, J.-L. Barrat, *Proc. Natl. Acad. Sci. USA* **2009**, *106*, 15113–15118.
- [23] P. L. Kapitza, *J. Phys. USSR* **1941**, *4*, 181–210.
- [24] J. Park, J. Huang, W. Wang, C. J. Murphy, D. G. Cahill, *J. Phys. Chem. C* **2012**, *116*, 26335–26341.
- [25] D. Li, Y. Wu, P. Kim, L. Shi, P. Yang, A. Majumdar, *Appl. Phys. Lett.* **2003**, *83*, 2934–2936.
- [26] F. Yang, C. Dames, *Phys. Rev. B* **2013**, *87*, 035437.
- [27] P. B. Roder, S. Manandhar, A. Devaraj, D. E. Perea, E. J. Davis, P. J. Pauzauskie, *J. Phys. Chem. C* **2016**, *120*, 21730–21739.
- [28] C. Cheng, W. Fan, J. Cao, S.-G. Ryu, J. Ji, C. P. Grigoropoulos, J. Wu, *ACS Nano* **2011**, *5*, 10102–10107.
- [29] O. M. Wilson, X. Hu, D. G. Cahill, P. V. Braun, *Phys. Rev. B* **2002**, *66*, 224301.
- [30] Z. B. Ge, D. G. Cahill, P. V. Braun, *J. Phys. Chem. B* **2004**, *108*, 18870–18875.
- [31] D. G. Cahill, P. V. Braun, G. Chen, D. R. Clarke, S. Fan, K. E. Goodson, P. Keblinski, W. P. King, G. D. Mahan, A. Majumdar, H. J. Maris, S. R. Philpot, E. Pop, L. Shi, *Appl. Phys. Rev.* **2014**, *1*, 011305.
- [32] L. Meng, R. Yu, M. Qiu, F. J. García de Abajo, *ACS Nano* **2017**, *11*, 7915–7924.
- [33] P. B. Roder, P. J. Pauzauskie, E. J. Davis, *Langmuir* **2012**, *28*, 16177–16185.
- [34] M. Kerker, *The Scattering of Light and Other Electromagnetic Radiation*, Academic Press, **1969**.
- [35] C. F. Bohren, D. R. Huffman, *Absorption and Scattering of Light by Small Particles*, Wiley-VCH, Weinheim, **1998**.
- [36] T. W. Odom, G. C. Schatz, *Chem. Rev.* **2011**, *111*, 3667–3668.
- [37] A. Agrawal, I. Krieger, D. J. Milliron, *J. Phys. Chem. C* **2015**, *119*, 6227–6238.
- [38] M. J. Rozin, D. A. Rosen, T. J. Dill, A. R. Tao, *Nat. Commun.* **2015**, *6*, 7325.
- [39] C. L. Baldwin, N. W. Bigelow, D. J. Masiello, *J. Phys. Chem. Lett.* **2014**, *5*, 1347–1354.
- [40] S. C. Nguyen, Q. Zhang, K. Manthiram, X. Ye, J. P. Lomont, C. B. Harris, H. Weller, A. P. Alivisatos, *ACS Nano* **2016**, *10*, 2144–2151.
- [41] B. Zhou, B. Shi, D. Jin, X. Liu, *Nat. Nanotechnol.* **2015**, *10*, 924–936.
- [42] X. Liu, C.-H. Yan, J. A. Capobianco, *Chem. Soc. Rev.* **2015**, *44*, 1299–1301.
- [43] A. Einstein, *Ann. Phys.* **1905**, *322*, 549–560.
- [44] A. Einstein, *Ann. Phys.* **1906**, *324*, 371–381.
- [45] R. B. Bird, W. E. Stewart, E. N. Lightfoot, D. J. Klingenberg, *Introductory Transport Phenomena*, Wiley, Hoboken, **2014**.
- [46] A. J. Mork, E. M. Y. Lee, W. A. Tisdale, *Phys. Chem. Chem. Phys.* **2016**, *18*, 28797–28801.
- [47] M. Kerker, *The Scattering of Light and Other Electromagnetic Radiation*, Elsevier, Amsterdam, **2016**.
- [48] C. Bohren, D. Huffman, *Wiley Interscience* **1983**, *13*, 123–127.
- [49] B. T. Draine, P. J. Flatau, *J. Opt. Soc. Am. A* **1994**, *11*, 1491.
- [50] A. M. Chockla, V. C. Holmberg, B. A. Korgel, *J. Phys. Chem. C* **2012**, *116*, 22625–22630.
- [51] A. F. Oskooi, D. Roundy, M. Ibanescu, P. Bermel, J. D. Joannopoulos, S. G. Johnson, *Comput. Phys. Commun.* **2010**, *181*, 687–702.
- [52] See ref. [33].
- [53] S. D. Lounis, E. L. Runnerstrom, A. Bergerud, D. Nordlund, D. J. Milliron, *J. Am. Chem. Soc.* **2014**, *136*, 7110–7116.
- [54] J. Wang, R. Deng, M. A. MacDonald, B. Chen, J. Yuan, F. Wang, D. Chi, T. S. Andy Hor, P. Zhang, G. Liu, Y. Han, X. Liu, *Nat. Mater.* **2014**, *13*, 157–162.
- [55] J. Zhang, D. Li, R. Chen, Q. Xiong, *Nature* **2013**, *493*, 504–508.
- [56] A. Pant, B. E. Smith, M. J. Crane, X. Zhou, M. B. Lim, S. A. Frazier, E. J. Davis, P. J. Pauzauskie, *J. Phys. Chem. C* **2018**, *122*, 7525–7532.
- [57] O. Svelto, D. C. Hanna, *Principles of Lasers*, Springer, **1998**.
- [58] See ref. [15].
- [59] See ref. [16].
- [60] P. B. Roder, B. E. Smith, E. J. Davis, P. J. Pauzauskie, *J. Phys. Chem. C* **2014**, *118*, 1407–1416.
- [61] P. O. A. L. Davies, M. J. Fisher, *Proc. R. Soc. London A* **1964**, *280*, 486–527.

- [62] M. J. Crane, B. E. Smith, P. B. Meisenheimer, X. Zhou, R. M. Stroud, E. J. Davis, P. J. Pauzauskie, *Diam. Relat. Mater.* **2018**, *87*, 134–142.
- [63] T. M. Allen, M. F. Buehler, E. J. Davis, *J. Colloid Interface Sci.* **1991**, *142*, 343–356.
- [64] H. M. L. Robert, F. Kundrat, E. Bermúdez-Ureña, H. Rigneault, S. Monneret, R. Quidant, J. Polleux, G. Baffou, *ACS Omega* **2016**, *1*, 2–8.
- [65] B. E. Smith, X. Zhou, E. J. Davis, P. J. Pauzauskie, *Opt. Eng.* **2017**, *56*, 011111–011117.
- [66] S. Chu, *Rev. Mod. Phys.* **1998**, *70*, 685–706.
- [67] M. Anderson, J. Ensher, M. Matthews, C. Wieman, E. Cornell, *Science* **1995**, *269*, 198–201.
- [68] P. Pringsheim, *Z. Phys.* **1929**, *57*, 739–746.
- [69] L. Landau, *J. Phys. Moscow* **1946**, *10*, 503–506.
- [70] A. Kastler, *J. Phys. Radium* **1950**, *11*, 255–265.
- [71] T. Kushida, J. E. Geusic, *Phys. Rev. Lett.* **1968**, *21*, 1172–1175.
- [72] R. Epstein, M. Buchwald, B. Edwards, T. Gosnell, C. Mungan, *Nature* **1995**, *377*, 500–503.
- [73] J. Thiede, J. Distel, S. R. Greenfield, R. I. Epstein, *Appl. Phys. Lett.* **2005**, *86*, 154107.
- [74] J. Fernández, A. Mendioroz, A. J. García, R. Balda, J. L. Adam, M. A. Ariandiaga, *Opt. Mater.* **2001**, *16*, 173–179.
- [75] J. Fernández, A. Mendioroz, A. J. García, R. Balda, J. L. Adam, *Phys. Rev. B* **2000**, *62*, 3213–3217.
- [76] S. R. Bowman, C. E. Mungan, *Appl. Phys. B* **2000**, *71*, 807–811.
- [77] G. Nemova, R. Kashyap, International Society for Optics And Photonics, **2015**, p. 938008.
- [78] R. I. Epstein, J. J. Brown, B. C. Edwards, A. Gibbs, *J. Appl. Phys.* **2001**, *90*, 4815–4819.
- [79] S. Bigotta, D. Parisi, L. Bonelli, A. Toncelli, M. Tonelli, A. Di Lieto, *J. Appl. Phys.* **2006**, *100*, 013109.
- [80] D. V. Seletskiy, S. D. Melgaard, S. Bigotta, A. Di Lieto, M. Tonelli, M. Sheik-Bahae, *Nat. Photonics* **2010**, *4*, 161–164.
- [81] S.-T. Ha, C. Shen, J. Zhang, Q. Xiong, *Nat. Photonics* **2016**, *10*, 115–121.
- [82] S. D. Melgaard, A. R. Albrecht, M. P. Hehlen, M. Sheik-Bahae, *Sci. Rep.* **2016**, *6*, 20380.
- [83] X. L. Ruan, M. Kaviani, *Phys. Rev. B* **2006**, *73*, 155422.
- [84] J. L. Clark, G. Rumbles, *Phys. Rev. Lett.* **1996**, *76*, 2037–2040.
- [85] K. Kroy, *Nat. Nanotechnol.* **2014**, *9*, 415–417.
- [86] A. T. M. A. Rahman, P. F. Barker, *Nat. Photonics* **2017**, *11*, 634.
- [87] Q. Liu, W. Feng, T. Yang, T. Yi, F. Li, *Nat. Protoc.* **2013**, *8*, 2033–2044.
- [88] L. Wang, Y. Li, *Nano Lett.* **2006**, *6*, 1645–1649.
- [89] T. J. Milstein, D. M. Kroupa, D. R. Gamelin, *Nano Lett.* **2018**, *18*, 3792–3799.
- [90] R. B. Wilson, D. G. Cahill, *Nat. Commun.* **2014**, *5*, 5075.
- [91] P. Reddy, K. Castelino, A. Majumdar, *Appl. Phys. Lett.* **2005**, *87*, 211908.
- [92] H. Wang, Y. Xu, M. Shimono, Y. Tanaka, M. Yamazaki, *Mater. Trans.* **2007**, *48*, 2349–2352.
- [93] J. Lombard, F. Detcheverry, S. Merabia, *J. Phys. Condens. Matter* **2015**, *27*, 015007.
- [94] E. J. McLaurin, L. R. Bradshaw, D. R. Gamelin, *Chem. Mater.* **2013**, *25*, 1283–1292.
- [95] E. Pop, *Nano Res.* **2010**, *3*, 147–169.
- [96] A. J. Mork, E. M. Y. Lee, N. S. Dahod, A. P. Willard, W. A. Tisdale, *J. Phys. Chem. Lett.* **2016**, *7*, 4213–4216.
- [97] G. Nemova, R. Kashyap, *Phys. Rev. A* **2011**, *83*, 013404.
- [98] G. Nemova, R. Kashyap, *JOSA B* **2012**, *29*, 676–682.
- [99] J. B. Khurgin, *Phys. Rev. Lett.* **2007**, *98*, 177401.
- [100] B. L. Lev, A. Vukics, E. R. Hudson, B. C. Sawyer, P. Domokos, H. Ritsch, J. Ye, *Phys. Rev. A* **2008**, *77*, 023402.

Manuscript received: February 13, 2018

Revised manuscript received: June 8, 2018

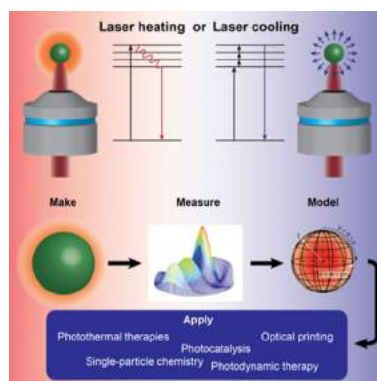
Accepted manuscript online: June 11, 2018

Version of record online: ■■■■■ 0000



## FOCUS REVIEW

**Taking a cold, hard look at nanostructures:** Recent advances have shown that lasers can photothermally heat and, surprisingly, cool nanostructures. This review focuses on modeling electro-magnetic absorption and heat transport in nanomaterials for laser-induced heating and cooling and discusses future directions for identifying and engineering new materials for laser cooling.



### Heat Transfer

Matthew J. Crane, Xuezhe Zhou,  
E. James Davis, Peter J. Pauzauskie\*

■■ – ■■

### Photothermal Heating and Cooling of Nanostructures